

# Evolved Neuromorphic Control for High Speed Divergence-based Landings of MAVs

Jesse J. Hagedaars<sup>1</sup>, Federico Paredes-Vallés<sup>1</sup>, Sander M. Bohté<sup>2</sup>, and Guido C.H.E. de Croon<sup>1</sup>

**Abstract**—Flying insects are capable of vision-based navigation in cluttered environments, reliably avoiding obstacles through fast and agile maneuvers, while being very efficient in the processing of visual stimuli. Meanwhile, autonomous micro air vehicles still lag far behind their biological counterparts, displaying inferior performance with a much higher energy consumption. In light of this, we want to mimic flying insects in terms of their processing capabilities, and consequently apply gained knowledge to a maneuver of relevance. This letter does so through evolving spiking neural networks for controlling landings of micro air vehicles using the divergence of the optical flow field of a downward-looking camera. We demonstrate that the resulting neuromorphic controllers transfer robustly from a highly abstracted simulation to the real world, performing fast and safe landings while keeping network spike rate minimal. Furthermore, we provide insight into the resources required for successfully solving the problem of divergence-based landing, showing that high-resolution control can potentially be learned with only a single spiking neuron. To the best of our knowledge, this is the first work integrating spiking neural networks in the control loop of a real-world flying robot. Videos of the experiments can be found at <http://bit.ly/neuro-controller>.

**Index Terms**—Aerial systems: perception and autonomy, autonomous vehicle navigation, spiking neural networks, neuromorphic computing, evolutionary algorithms.

## I. INTRODUCTION

Flying insects are everything we would like micro air vehicles (MAVs) to be: units that can navigate autonomously in cluttered environments through fast and agile maneuvers, despite being strongly limited in computational and energy resources. Like most animals that can see, these insects rely heavily on patterns of visual motion, or *optical flow* [1], for many important behaviors. During landing, for instance, honeybees maintain a constant rate of expansion, or *divergence*, of the optical flow field to ensure a smooth approach [2].

Insects perceive visual motion in a *spike-based* manner through light-sensitive cells and networks of interconnected neurons that react to brightness changes in the environment [3]. The sparsity and asynchronicity of such a spike-driven approach have inspired researchers to come up with artificial substitutes, referred to as *neuromorphic*, that could potentially be used by insect-scale MAVs [4], [5] for efficient

vision-based navigation. Event cameras [6], whose pixels register brightness changes as events, take the place of the retina. *Spiking neural networks* (SNNs) [7] assume the role of the underlying networks, subsequently transforming these event streams into estimates of visual motion.

Although the interest for event cameras is growing rapidly in the field of robotics [6], SNNs have not yet become widespread in control applications. The cause of this lies partially in the difficulty of training: the discrete spiking nature of SNNs severely limits the use of gradient-based optimization algorithms. Instead, most learning is based on the relative timing of spikes [8], often in combination with a surrogate gradient [9], [10] or global reward signal [11], [12] to allow the specification of desired behavior or goals. As far as robot control is concerned, these learning rules currently seem to be limited to simulated applications [13], [14] or simpler, discrete real-world problems [15].

*Artificial neural networks* (ANNs), on the other hand, have been employed successfully for real-world, vision-based continuous control. For instance, [16] used an *evolutionary* algorithm to optimize ANNs for performing divergence-based landings of MAVs. Solving the same control problem, but replacing the ANNs with SNNs, this work aims to demonstrate that SNNs can likewise be taught to perform such a task using evolutionary learning, or *neuroevolution* [17]. The generality of the evolutionary framework, both in terms of suitable problems [18] as well as the structure and characteristics of the evolved individuals [19], adds to the promise of this approach.

This letter contains two main contributions. First, we demonstrate learned neuromorphic control based on optical flow for the real-world, continuous problem of divergence-based landing of an MAV, with learning taking place in a highly abstracted simulation environment. Second, we study how to substantially reduce the spike rate of the SNN controller, corresponding to considerable energy savings if it were to be run on neuromorphic hardware. Besides investigating the effect of pruning neurons (as also done in [20], [21]), we introduce the inclusion of network spike rate as an objective in the multi-objective neuroevolution.

The remainder of this letter is structured as follows. Section II provides related work concerning neuromorphic controllers and neuroevolution for robotics. The control problem, SNN configuration, neuroevolutionary procedure, and simulation environment are discussed in Section III. Next, Section IV goes over the setup of the performed experiments and lists their findings. Conclusions drawn from these findings are then stated in Section V.

<sup>1</sup>J. J. Hagedaars, F. Paredes-Vallés, and G. C. H. E. de Croon are with the Micro Air Vehicle Laboratory, Department of Control and Simulation, Faculty of Aerospace Engineering, Delft University of Technology, 2629HS Delft, The Netherlands (email: [jessehagedaars@gmail.com](mailto:jessehagedaars@gmail.com); [f.paredesvalles@tudelft.nl](mailto:f.paredesvalles@tudelft.nl); [g.c.h.e.decroon@tudelft.nl](mailto:g.c.h.e.decroon@tudelft.nl)) (corresponding author: J. J. Hagedaars).

<sup>2</sup>S. M. Bohté is with the Machine Learning Group, Centrum Wiskunde & Informatica, 1098XG Amsterdam, The Netherlands (email: [s.m.bohte@cwi.nl](mailto:s.m.bohte@cwi.nl)).

## II. RELATED WORK

### A. Neuromorphic Robot Controllers

Neuromorphic control (i.e., control using SNNs) can either be learned or hand-engineered. Whereas the latter approach already lends itself for more sophisticated control tasks, fully learned controllers have so far only been implemented for simpler or simulated problems. For instance, [22], [23] demonstrate real-world vision-based control of a wheeled robot, but their SNNs are largely made up of hand-designed and hand-tuned neuronal populations and connections. In [15], a reward-modulated rule is used to learn most weights of an SNN, but only for a simplified and discrete obstacle avoidance problem with an MAV.

Regarding simulation, [14] shows fully learned vision-based neuromorphic control for lane-keeping. Events coming from an event camera excite a population of neurons, whose spikes are fed to a two-neuron SNN that outputs motor speeds for a two-wheeled robot. Although synaptic weights are learned through reward-modulated learning, the task is set up in such a way that its complexity remains limited: rewards are tailored to each individual neuron, so that increased firing inevitably results in a self-centering policy. In [13], the authors employ the same learning rule and a three-layer SNN for learning flight control of a simulated robotic insect. In this case, reward is based on the deviation from the flight trajectory generated by a linear quadratic regulator, making it essentially a lane-keeping task similar to [14].

### B. Neuroevolution for Robot Control

Reviews of the field of neuroevolution show the feasibility of using this technique for learning in ANNs [24] and SNNs [17]. Apart from scaling well in terms of compute, neuroevolution proved to often be more sample efficient than reinforcement learning approaches [24]. Additionally, the population-based framework of evolution inherently promotes behavioral diversity in case of multiple objectives [24] and can be used for the optimization of all parameters of a network, including learning rule characteristics [25].

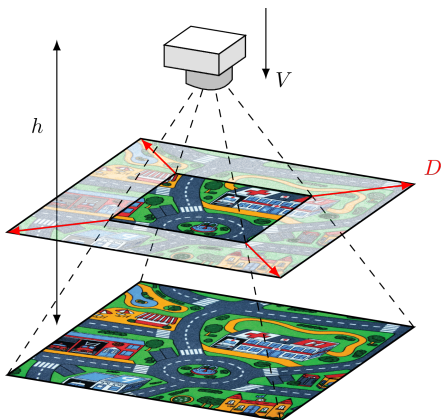


Fig. 1. Illustration of optical flow divergence. As the camera moves towards the surface, its field-of-view covers a smaller portion of the original pattern, and distances between any two points on the camera’s pixel array increase. This increase is proportional to the divergence  $D$ .

Regarding evolutionary robotics, [16] demonstrates real-world optical flow control of a landing MAV, where the ANN controller was evolved offline. A shallow network was sufficient to perform continuous control, with only the weights being evolved.

The number of recent real-world applications involving neuroevolution for SNN controllers is limited. The authors of [26], [27] evolve SNNs for the control of a two-wheeled robot based on basic vision (e.g., light sensors). In [28], a walking task for a six-legged robot is learned offline, after which the learned policy is transferred to the real world. There seems to little consensus about the to-be-evolved parameters of the SNN: some mainly evolve the topology of the network, while others evolve the weights and hyperparameters.

## III. METHODOLOGY

### A. Divergence of the Optical Flow Field

In this work, we use the efficient optical flow formulation from [29], which assumes a downward-looking camera moving over a static planar surface, as depicted in Fig. 1. With this configuration, moving the camera along the positive  $Z$ -axis (as is the case for vertical landings of MAVs) causes an optical flow, in this case divergence, to be perceived. Physically, divergence corresponds to the ratio of vertical velocity and height above the surface, or  $D = V/h$ .

We employ an alternative method, in which divergence is estimated through the relative, temporal variation in the distance between any two image points [30]. Referred to as *size divergence*  $D_s$ , this method results in a reliable estimate of divergence, denoted by  $\hat{D}$ , when averaged over a set of  $N_D$  pairs of points:

$$D_s(t) = \frac{1}{\Delta t} \frac{l(t) - l(t - \Delta t)}{l(t - \Delta t)} \quad (1)$$

$$\hat{D}(t) = \frac{1}{N_D} \sum_{i=1}^{N_D} D_s(t)$$

### B. Spiking Neural Network Architecture

In SNNs, neurons are connected through *synapses*, which have a certain weight. The neuron on the receiving end of a synapse is named *postsynaptic*, while the transmitting neuron is referred to as *presynaptic*. Incoming spikes contribute to the *membrane potential*  $u_i(t)$  of a neuron in an additive (*excitatory*) or subtractive (*inhibitory*) manner. In case no inputs are received,  $u_i(t)$  decays to a resting potential  $u_{rest}$ . On the other hand, if the quantity of inputs is large enough to push the potential above a threshold  $\theta_i$ , the neuron itself emits a spike  $s_i$ , after which the potential is reset to  $u_{rest}$ .

The neuron model employed in this work is the often-used *leaky integrate-and-fire* (LIF) [31]. The continuous neuronal dynamics of this model can be discretized using forward Euler, which leaves us with the following equation for the membrane potential:

$$u_i(t) = u_i(t - \Delta t) \cdot \tau_{u_i} + \alpha_{u_i} i_i(t) \quad (2)$$

where we assumed  $u_{rest} = 0$ , and take the membrane decay as a factor  $\tau_{u_i}$ .  $i_i(t)$  is the forcing function working on the postsynaptic neuron  $i$ , which corresponds to the presynaptic spikes multiplied by their respective synaptic weights, i.e.,  $i_i(t) = \sum_j w_{ij} s_j(t)$ , or to presynaptic currents  $c_j(t)$ , i.e.,  $i_i(t) = \sum_j w_{ij} c_j(t)$ . The influence of the forcing function on the membrane potential is scaled with a constant  $\alpha_{u_i}$ .

To prevent excessive firing while ensuring responsiveness to small inputs (e.g. small currents or low-frequency signals),  $\theta_i$  can be made dependent on the neuron's firing rate, resulting in an adaptive LIF [32]:

$$\theta_i(t) = \theta_i(t - \Delta t) \cdot \tau_{\theta_i} + \alpha_{\theta_i} s_i(t) \quad (3)$$

with  $\tau_{\theta_i}$  being the corresponding decay factor, and  $\alpha_{\theta_i}$  the constant scaling the postsynaptic spikes.

The binary nature of SNNs requires functions that transform real-valued signals to binary spikes and vice-versa, i.e., *encodings* and *decodings*. This work makes use of a pair of non-spiking neurons per input observation, one for positive and one for negative values. These neurons give off a proportional current, with at most one of the two neurons being active at a given time. More specifically, the current  $c_i(t)$  coming out of each neuron can be expressed as:

$$c_i(t) = |f(o_i(t))| \quad (4)$$

where  $o_i(t)$  is the observation variable belonging to neuron  $i$ , and  $f(\cdot)$  is a clamping function:  $\min(0, \cdot)$  for the negative neuron, and  $\max(0, \cdot)$  for the positive.

For decoding binary spikes to real-valued scalars  $a_i(t)$  (actions) in a range  $[r_1, r_2]$ , the postsynaptic *trace*  $X_i(t)$ , which is essentially a low-pass filter over postsynaptic spikes, can be combined with a simple scaling:

$$\begin{aligned} a_i(t) &= r_1 + (r_2 - r_1) \cdot X_i(t) \\ X_i(t) &= X_i(t - \Delta t) \cdot \tau_{x_i} + \alpha_{x_i} s_i(t) \end{aligned} \quad (5)$$

The SNN used for the control task in this work is kept relatively simple, with only a single hidden layer of not more than 20 adaptive LIF neurons, and a single output LIF neuron. We consider vertical control to be one-dimensional, with the SNN controller setting the thrust.

### C. Evolving Energy-efficient Neuromorphic Controllers

Each evolution starts off with a randomly initialized *population* of  $\mu$  SNN individuals. We opt for a *mutation-only* approach, given that crossover tends to work best when natural building blocks are available, and could lead to difficulties like the permutation problem when applied to neural networks [33]. Weights and hyperparameters are mutated with  $P_{mut} = 0.3$  according to the distributions in Table I. *Offspring*  $\lambda$  is combined with the previous population and evaluated in a highly stochastic simulation environment (see Section III-D), where the repeated evaluation of the previous generation decreases the chance individuals live on only because they received ‘easy’ environmental conditions. The *fitness* of an individual consists of four objectives: time to land ( $f_1$ ), final height ( $f_2$ ), final vertical velocity ( $f_3$ ), and

TABLE I  
SAMPLING DISTRIBUTIONS OF MUTATED PARAMETERS

Parameter	Distribution
$w_{ij}$	$\mathcal{U}(-w_{ij} - 0.05, 2w_{ij} + 0.05)$
$\alpha_{u_i}, \alpha_{\theta_i}, \alpha_{x_i}$	$\mathcal{U}(\alpha - 2/3, \alpha + 2/3)$ , clamped to $[0, 2]$
$\tau_{u_i}, \tau_{\theta_i}, \tau_{x_i}$	$\mathcal{U}(\tau - 1/3, \tau + 1/3)$ , clamped to $[0, 1]$
$\theta_i$	$\mathcal{U}(\theta_i - 1/3, \theta_i + 1/3)$ , clamped to $[0, 1]$

total spike rate of the network ( $f_4$ ). Selection is carried out using the multi-objective genetic algorithm *MSGA-II* [34].

During evolution, a *hall of fame* is maintained, which contains the all-time Pareto front of best individuals. After  $N_{gen}$  generations, all individuals in this group are evaluated by letting them perform 250 landings and quantifying the median and inter-quartile range (IQR) for each evolutionary objective. Then, the best-performing individuals are selected. So even though the hall of fame may still contain individuals that got ‘lucky’ during evolution, these will be identified and disregarded during the subsequent evaluation.

### D. Randomized Vertical Simulation Environment

The vertical simulation environment in which individuals are evaluated makes use of domain randomization and artificial noise to improve transferability to the real world. The available observations are the divergence  $\hat{D}$  and its temporal derivative  $\Delta \hat{D}$ . Similarly to [16], the simulated MAV is considered as a unit mass under the influence of gravity, and control happens in one dimension with the SNN controller selecting a thrust setpoint  $T_{sp}$ . This leads to the following dynamics model:

$$\begin{aligned} h(t) &= h(t - \Delta t) + \Delta t \cdot v(t - \Delta t) \\ v(t) &= v(t - \Delta t) + \Delta t \cdot T(t - \Delta t) + w(t) \\ T(t) &= T(t - \Delta t) + \Delta t \cdot \frac{T_{sp} \cdot g - T(t - \Delta t)}{\Delta t + \tau_T} \end{aligned} \quad (6)$$

where the altitude  $h$ , vertical velocity  $v$ , and thrust  $T$  are updated using the forward Euler method, and  $\tau_T$  represents the spin-up and spin-down time of the rotors. The thrust setpoint  $T_{sp}$  selected by the SNN is clamped to a realistic range of acceleration for the MAV, namely  $[-0.8, 0.5]$  g. Lastly,  $w$  denotes vertical wind, and is given by:

$$w(t) = w(t - \Delta t) + \Delta t \cdot \frac{\mathcal{N}(0, \sigma_{wind}^2) - w(t - \Delta t)}{\Delta t + \sigma_{wind}} \quad (7)$$

with  $\sigma_{wind} = 0.1 \text{ ms}^{-1}$  being the standard deviation of the normally distributed wind.

Noise is added to the divergence estimation according to the model in [35]. The observed divergence  $\hat{D}$  is the result of adding a delay  $\delta_D$  to the ground-truth divergence, along with white noise and proportional white noise:

$$\begin{aligned} \hat{D}(t) &= D(t - \delta_D \cdot \Delta t) + \mathcal{N}(0, \sigma_D^2) \\ &\quad + D(t - \delta_D \cdot \Delta t) \cdot \mathcal{N}(0, \sigma_{D_{prop}}^2) \end{aligned} \quad (8)$$

where  $\sigma_D$  and  $\sigma_{D_{prop}}$  are the standard deviations for the added noise and proportional noise, respectively. Additionally, computational jitter is introduced in order to simulate

TABLE II  
SAMPLING DISTRIBUTIONS OF ENVIRONMENT PARAMETERS

Parameter	Distribution
$\delta_D$	$\mathcal{U}(1, 4)$ steps
$\sigma_D$	$\mathcal{U}(0.05, 0.15) \text{ s}^{-1}$
$\sigma_{D_{prop}}$	$\mathcal{U}(0.0, 0.25) \text{ s}^{-1}$
$\tau_T$	$\mathcal{U}(0.005, 0.04) \text{ s}$
$\Delta t$	$\mathcal{U}(0.02, 0.0333) \text{ s}$
$P_{jitter}$	$\mathcal{U}(0.0, 0.2)$

the case in which the estimated divergence is not updated due to, for instance, insufficient corner points. Each time step, there is the probability  $P_{jitter}$  that the estimated divergence from the previous step is used (for a maximum of one step).

The evaluation of an individual consists of four landings, from initial altitudes  $h_0 = 2, 4, 6, 8$  m. The environment is bounded in altitude and time:  $[0.05, h_0 + 5]$  m and 30 s, respectively. Individuals start out without initial velocity and acceleration, and are left to settle for 0.5 s. Each landing has its own, differently randomized environment, with parameters (as in Table II) being redrawn at the start of each generation, such that all individuals experience the same four environments. Fitness is averaged across the four landings, with individuals that do not manage to land receiving extra punishment.

#### IV. EXPERIMENTS

##### A. Experimental Setup

1) *Simulation*: Per configuration, four randomly initialized populations of 100 individuals are evolved for 400 generations, after which their final halls of fame are combined. Initial synaptic weights are drawn from  $\mathcal{U}(0, 1)$ , and other hyperparameters are initialized as constants:  $(\alpha_{u_i}, \alpha_{\theta_i}, \alpha_{x_i}) = (0.2, 0.2, 1.0)$ ,  $(\tau_{u_i}, \tau_{\theta_i}, \tau_{x_i}) = (0.8, 0.8, 0.8)$ , and  $\theta_i = 0.2$ .

Simulations are carried out in Python 3.6 on a laptop running Ubuntu 18.04 LTS, equipped with an Intel i7-7700HQ quad-core CPU and 16 GB of memory. For simulating SNNs, we used the open-source PySNN<sup>1</sup> library; for performing the evolutions, we used the DEAP [36] framework. The code for running the experiments<sup>2</sup> and the simulation environment<sup>3</sup> is also publicly available.

2) *Real World*: The MAV used in this work is a Parrot Bebop 2 running the open-source Paparazzi<sup>4</sup> autopilot on its 780 MHz dual-core ARM Cortex A9 processor. Landings start from an initial altitude of roughly 4 m. Horizontal guidance and ground-truth measurements are provided by a motion capture system. Similar to [16], [37], divergence is estimated as size divergence using the Bebop’s downward-looking CMOS camera, and a FAST corner detector [38] in combination with a pyramidal Lucas-Kanade feature tracker [39]. To limit computational expense,  $N_D$  is capped

<sup>1</sup>Available at <https://github.com/BasBuller/PySNN>

<sup>2</sup>Available at <https://github.com/Huizerd/evolutionary>

<sup>3</sup>Available at <https://github.com/Huizerd/gym-quad>

<sup>4</sup>Available at <https://github.com/paparazzi/paparazzi>

at 100 points. Divergence measurements are updated at a rate of approximately 45 Hz, while the custom vertical control loop implementing the divergence-based landing runs at roughly 512 Hz.

To run the SNN on board we developed TinySNN<sup>5</sup>: a framework for building small spiking networks in the C programming language. This framework, which is based on PySNN, allows an almost seamless transfer of networks from simulation to the real-world hardware.

As discussed in [16], linearly transforming the thrust setpoint  $T_{sp}$  to rotor commands leads to poor tracking performance due to unmodeled drag and nonlinear aerodynamic effects that result from a descent through the propeller downwash. To close this reality gap, a PI controller (with gains  $P = 0.7$  and  $I = 0.3$ ) was used to convert the thrust setpoint to motor commands, as suggested by [40].

##### B. 20 Hidden Neurons

The first SNN configuration considered here is *20-base*, which has 20 adaptive LIF neurons as hidden layer. Fig. 2 displays the Pareto front of evolved individuals for this configuration in red. From this front, a single individual, indicated by a bold circle, is selected for further testing. Note that objective  $f_2$  (final altitude) is not shown in Fig. 2, as this was almost consistently minimized for all individuals.

Looking at the simulated landings performed by this individual in Fig. 3a, we see that most landings are quite smooth (low touchdown velocity), except for maybe one. The plots of thrust setpoint  $T_{sp}$ , however, show high-frequency oscillations, with a magnitude almost as large as the allowed acceleration range  $[-0.8, 0.5]$  g. This behavior is caused by the values of  $\alpha_{x_i}$  and  $\tau_{x_i}$  of the decoding, which cause instantaneous jumps and decays to maximum and (almost) minimum acceleration, respectively. Controllers that show this kind of behavior are called *on-off* or *bang-bang* controllers, and [16] argues that these are unlikely to transfer

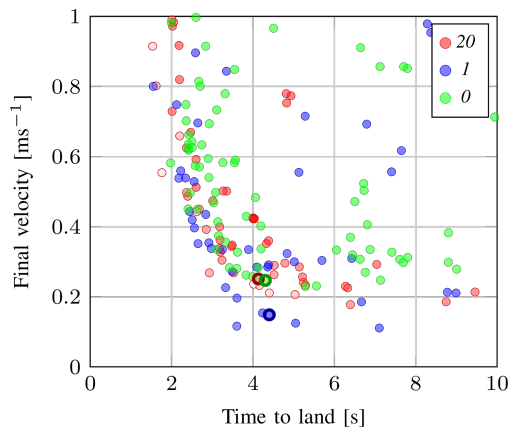
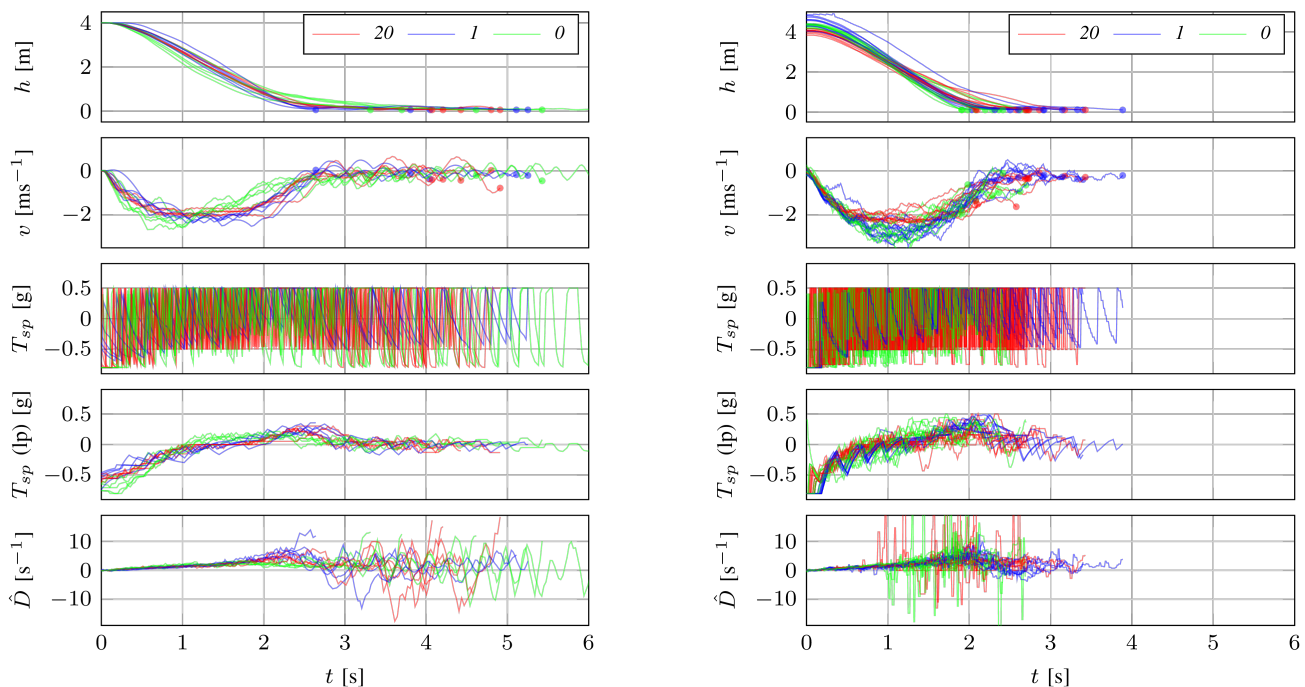


Fig. 2. Pareto front (based on median performance over 250 evaluations) of individuals in the final hall of fame for *20-base*, *1-lim*, and *0-lim*. The dot’s color shade is proportional to the spike rate median: lighter means a higher rate. Selected individuals are indicated in bold.

<sup>5</sup>Available at <https://github.com/Huizerd/tinysnn>



(a) Five simulated runs in a randomized environment.

(b) Ten real-world flight tests.

Fig. 3. Height, velocity, thrust setpoint (raw and 20-step moving average), and estimated divergence for simulated and real-world landings of selected individuals from *20-base*, *1-lim*, and *0-lim* (see Fig. 2). Dots in the  $h$  and  $v$  plot mark the end of runs.

well from simulation to the real world. The cause of this lies in the fact that this kind of control, which involves quick alternation of spinning up and spinning down the rotors, is highly dependent on motor dynamics (spin-up and spin-down time  $\tau_T$ ). These dynamics are almost certainly different for simulation and real world, resulting in bad transfers.

When taking the selected controller to the real world, we can conclude from Fig. 3b that this is indeed so, with higher touchdown velocities and quicker landings (2-3 s in reality versus 5-6 s in simulation). The quick oscillations in  $T_{sp}$  cannot be followed by the motors, leading to lower values of acceleration than actually desired. Currently, the evolutionary process has little way of accounting for this discrepancy, because the bang-bang control leads to good landings in simulation. In the next section, we therefore constrain the mutation of  $\alpha$ 's (mutation magnitude halved, clamped to  $[0, 1]$ ) and  $\tau$ 's (clamped to  $[0.3, 1]$ ), decreasing the chances that bang-bang control will emerge.

During the simulated landings of Fig. 3a, the spiking activity of each neuron was recorded. Fig. 4 gives the average spike rate per neuron, as well as the sign and magnitude of the connections. The majority of the hidden neurons of *20-base* (left network) are purple in color, meaning little activity. Combined with the fact that most connections are rather weak, this points to a certain redundancy regarding hidden neurons. Minimizing spike rate of the network therefore not only promotes energy-efficient data processing, but also gives insight into the resources required for solving a problem. The single yellow path from input to output layer, together with

the single effectively active neuron in the hidden layer, leads us to believe divergence-based landings can be performed with only a single spiking hidden neuron (*1-lim*), or possibly none at all (*0-lim*).

### C. One or No Hidden Neuron

Fig. 2 lets us compare the Pareto fronts for *20-base*, *1-lim* and *0-lim*, with the latter two limited in the mutation of  $\alpha$ 's and  $\tau$ 's. It immediately becomes clear that the front of *1-lim* outperforms those of the other cases. Most likely, this is the result of a combination of an increase in evolutionary resources available per neuron and the prevention of less-optimal parameter combinations by clamping  $\alpha$ 's and  $\tau$ 's. A quick comparison of *1-lim* and *0-lim* indicates that, while Pareto individuals from *0-lim* may be able to land successfully, having a hidden layer (even though it consists of only a single neuron) will lead to better performance.

The comparison of simulated landings in Fig. 3b shows that, even though all selected controllers perform roughly the same in terms of time to land, *1-lim* often touches down with less vertical velocity. Furthermore, as can be seen from the plots of  $T_{sp}$ , the control policy of *1-lim* is characterized by relatively slow decay and few output spikes. This leads to a desired thrust that is slowly varying most of the time, but which can increase suddenly through the emission of a spike, resulting in the small 'hops' in vertical velocity during descent. As the ground nears, the magnitude of these hops seems to decrease, leading to superior low-altitude control compared to *20-base* and *0-lim*. Nevertheless, the landings performed by the single-spiking-neuron controller *0-lim* also

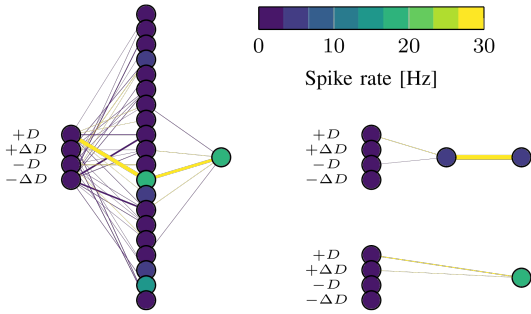


Fig. 4. Average firing rates and synaptic weights of selected individuals from *20-base* (left), *1-lim* (top right), and *0-lim* (bottom right) for the five simulated runs displayed in Fig. 3a. Total network spike rates are equal to 71.2 Hz, 7.5 Hz, and 16.8 Hz, respectively. Vertex color is proportional to neuron firing rate, while synaptic weight is directly proportional to edge weight in points. Edge colors indicate inhibitory (purple) or excitatory (yellow) synapses.

look promising. Like *1-lim*, decoding decay is slower, which allows a larger number of acceleration setpoints to be selected. Still, the high frequency and large magnitude of the oscillations will most likely prevent a good transfer to the real world. Looking at Fig. 3b, we see that this is indeed the case. The touchdown velocity of both *20-base* and *0-lim* is often higher than that of *1-lim*, whose slower decoding dynamics helped with a successful transfer from simulation to the real world.

The network activity during simulated landings in Fig. 4 indicates that, in the case of *0-lim*, further evolutionary optimization might decrease spike rate even more, as is shown to be feasible by the network of *1-lim*. Also, all networks seem to rely mainly on divergence  $\hat{D}$  for control, instead of its temporal derivative  $\Delta\hat{D}$ . More specifically, an indication of positive divergence alone might suffice, given that an absence of  $+\hat{D}$ -activity relates to  $-\hat{D}$ .

Fig. 5 compares the transient and steady-state response of (from left to right) *20-base*, *1-lim*, and *0-lim*. The transient response of *1-lim* shows a much larger number of possible thrust setpoints than any other individual, due to its slower decoding dynamics. Furthermore, it limits itself to a smaller  $T_{sp}$  range, preventing large-magnitude oscillations. Both *20-base* and *0-lim*, on the other hand, only have a distinct number of plateaus in their transient response, and these have to cover the entire range  $[-0.8, 0.5]$  g. Looking at the steady-state response, we see that *20-base* and *1-lim* mainly have a gradient in the  $\hat{D}$ -dimension, which makes sense given the connections in those networks to the respective encoding neuron. The response of *0-lim*, however, also has a significant gradient in the  $\Delta\hat{D}$ -dimension, as this individual additionally has an excitatory connection to the input neuron responsible for  $+\Delta\hat{D}$ .

Apart from giving insight into the strategies of individual controllers, Fig. 5 can tell us something about the difficulty and nature of the problem of divergence-based landing. Clearly, the transient responses of the individuals all take some kind of sigmoid shape, though it may be more of a half sigmoid for  $D \geq 0$ , and a sloped line for  $D < 0$ . In

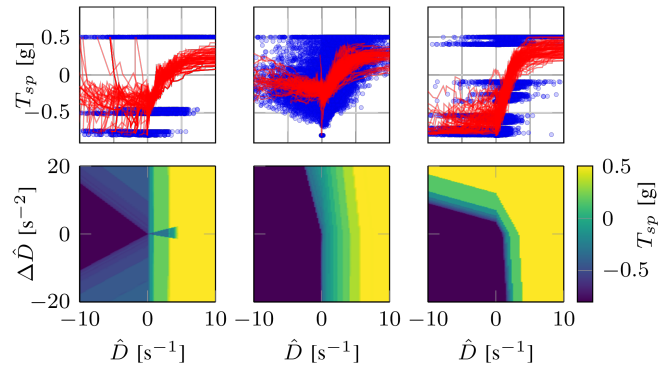


Fig. 5. Transient and steady-state response of selected individuals from *20-base* (left), *1-lim* (middle), and *0-lim* (right) as given in Fig. 2. Steady-state response is obtained by subjecting the SNNs to 100 time steps of the same observation and subsequently averaging the last 50 steps. The transient response is made up of 100 simulated landings during which  $D$  and  $T_{sp}$  are recorded (blue dots), and then sorted by increasing divergence and passed through a 40-step moving average (red lines).

comparison, the response given by a proportional divergence controller would be a straight line, with its slope dependent on the controller's gain. Clamping and offsetting such a P-controller might also give us comparable control strategies. The steady-state plot of such a controller would have an even gradient along  $D$ , plateauing at the thrust bounds.

The problem and its solution found by the SNN controllers in this work are certainly nonlinear, and not entirely trivial. Nevertheless, much simpler controllers, like those mentioned above, can now be made. The beauty of the approach in this work and in [16], however, is the emergence of these simpler control policies through learning, allowing us to come up with strategies not thought of before.

## V. CONCLUSION

In this letter, we demonstrated, for the first time, that neuromorphic controllers evolved in a highly abstracted simulation environment are capable of real-world, continuous control in the form of landing MAVs based on the divergence of the optical flow field. Further, by minimizing the amount of spikes during evolution, we provided insight into the resources required for successfully solving the problem at hand. As it turns out, SNNs with hidden layers of a single neuron or no hidden layer at all are also able to land smoothly, all the while doing so at a fraction of the spikes required. This is in line with [41], which implies that single biological neurons are capable of solving linearly non-separable problems. Future research should focus on achieving an end-to-end spiking solution to this problem. This could potentially be done by combining the neuromorphic controllers from this work with the SNN from [42], which was shown to be able to compress the stimuli captured by an event camera into global motion estimates.

## REFERENCES

- [1] J. J. Gibson, *The Perception of the Visual World*. Boston: Houghton Mifflin Company, 1950.

- [2] E. Baird, N. Boeddeker, M. R. Ibbotson, and M. V. Srinivasan, "A universal strategy for visually guided landing," *Proceedings of the National Academy of Sciences*, vol. 110, no. 46, pp. 18686–18691, Nov. 2013.
- [3] C. Posch, T. Serrano-Gotarredona, B. Linares-Barranco, and T. Delbruck, "Retinomorphonic Event-Based Vision Sensors: Bioinspired Cameras With Spiking Output," *Proceedings of the IEEE*, vol. 102, no. 10, pp. 1470–1484, Oct. 2014.
- [4] G. C. H. E. de Croon, K. M. E. de Clercq, R. Ruijsink, B. Remes, and C. de Wagter, "Design, Aerodynamics, and Vision-Based Control of the Delfly," *International Journal of Micro Air Vehicles*, vol. 1, no. 2, pp. 71–97, Jun. 2009.
- [5] K. Y. Ma, P. Chirarattananon, S. B. Fuller, and R. J. Wood, "Controlled Flight of a Biologically Inspired, Insect-Scale Robot," *Science*, vol. 340, no. 6132, pp. 603–607, May 2013.
- [6] G. Gallego, T. Delbruck, G. Orchard, C. Bartolozzi, B. Taba, A. Censi, S. Leutenegger, A. Davison, J. Conradt, K. Daniilidis, and D. Scaramuzza, "Event-based Vision: A Survey," *arXiv:1904.08405 [cs]*, Apr. 2019, arXiv: 1904.08405.
- [7] W. Maass, "Networks of spiking neurons: The third generation of neural network models," *Neural Networks*, vol. 10, no. 9, pp. 1659–1671, Dec. 1997.
- [8] N. Caporale and Y. Dan, "Spike Timing-Dependent Plasticity: A Hebbian Learning Rule," *Annual Review of Neuroscience*, vol. 31, no. 1, pp. 25–46, 2008.
- [9] S. M. Bohte, J. N. Kok, and H. La Poutr, "Error-backpropagation in temporally encoded networks of spiking neurons," *Neurocomputing*, vol. 48, no. 1, pp. 17–37, Oct. 2002.
- [10] S. B. Shrestha and G. Orchard, "SLAYER: Spike Layer Error Reassignment in Time," in *Advances in Neural Information Processing Systems 31*, S. Bengio, H. Wallach, H. Larochelle, K. Grauman, N. Cesa-Bianchi, and R. Garnett, Eds. Curran Associates, Inc., 2018, pp. 1412–1421.
- [11] R. V. Florian, "Reinforcement Learning Through Modulation of Spike-Timing-Dependent Synaptic Plasticity," *Neural Computation*, vol. 19, no. 6, pp. 1468–1502, Apr. 2007.
- [12] N. F. Frémaux, H. Sprekeler, and W. Gerstner, "Reinforcement Learning Using a Continuous Time Actor-Critic Framework with Spiking Neurons," *PLOS Computational Biology*, vol. 9, no. 4, p. e1003024, Apr. 2013.
- [13] T. S. Clawson, S. Ferrari, S. B. Fuller, and R. J. Wood, "Spiking neural network (SNN) control of a flapping insect-scale robot," in *2016 IEEE 55th Conference on Decision and Control (CDC)*, Dec. 2016, pp. 3381–3388.
- [14] Z. Bing, C. Meschede, G. Chen, A. Knoll, and K. Huang, "Indirect and direct training of spiking neural networks for end-to-end control of a lane-keeping vehicle," *Neural Networks*, vol. 121, pp. 21–36, Jan. 2020.
- [15] F. Zhao, Y. Zeng, and B. Xu, "A Brain-Inspired Decision-Making Spiking Neural Network and Its Application in Unmanned Aerial Vehicle," *Frontiers in Neurobotics*, vol. 12, 2018.
- [16] K. Y. W. Scheper and G. C. H. E. de Croon, "Evolution of robust high speed optical-flow-based landing for autonomous MAVs," *Robotics and Autonomous Systems*, vol. 124, p. 103380, Feb. 2020.
- [17] D. Floreano, P. Drr, and C. Mattiussi, "Neuroevolution: from architectures to learning," *Evolutionary Intelligence*, vol. 1, no. 1, pp. 47–62, Mar. 2008.
- [18] T. Bck, D. B. Fogel, and Z. Michalewicz, *Handbook of Evolutionary Computation*. CRC Press, Jan. 1997.
- [19] D. B. Fogel, "The Advantages of Evolutionary Computation," in *Biocomputing and Emergent Computation: Proceedings of BCEC97*. World Scientific Press, 1997, pp. 1–11.
- [20] J. Iglesias, J. Eriksson, F. Grize, M. Tomassini, and A. E. P. Villa, "Dynamics of pruning in simulated large-scale spiking neural networks," *Biosystems*, vol. 79, no. 1, pp. 11–20, Jan. 2005.
- [21] S. Dora, S. Sundaram, and N. Sundararajan, "A two stage learning algorithm for a Growing-Pruning Spiking Neural Network for pattern classification problems," in *2015 International Joint Conference on Neural Networks (IJCNN)*, Jul. 2015, pp. 1–7, iSSN: 2161-4393.
- [22] F. Galluppi, C. Denk, M. C. Meiner, T. C. Stewart, L. A. Plana, C. Eliasmith, S. Furber, and J. Conradt, "Event-based neural computing on an autonomous mobile platform," in *2014 IEEE International Conference on Robotics and Automation (ICRA)*, May 2014, pp. 2862–2867, iSSN: 1050-4729.
- [23] M. B. Milde, H. Blum, A. Dietmiller, D. Sumislawska, J. Conradt, G. Indiveri, and Y. Sandamirskaya, "Obstacle Avoidance and Target Acquisition for Robot Navigation Using a Mixed Signal Analog/Digital Neuromorphic Processing System," *Frontiers in Neurobotics*, vol. 11, 2017.
- [24] K. O. Stanley, J. Clune, J. Lehman, and R. Miikkulainen, "Designing neural networks through neuroevolution," *Nature Machine Intelligence*, vol. 1, no. 1, pp. 24–35, Jan. 2019.
- [25] M. Jaderberg, V. Dalibard, S. Osindero, W. M. Czarnecki, J. Donahue, A. Razavi, O. Vinyals, T. Green, I. Dunning, K. Simonyan, C. Fernando, and K. Kavukcuoglu, "Population Based Training of Neural Networks," *arXiv:1711.09846 [cs]*, Nov. 2017, arXiv: 1711.09846.
- [26] D. Floreano, J.-C. Zufferey, and J.-D. Nicoud, "From Wheels to Wings with Evolutionary Spiking Circuits," *Artificial Life*, vol. 11, no. 1-2, pp. 121–138, Jan. 2005.
- [27] R. Battlori, C. B. Laramée, W. Land, and J. D. Schaffer, "Evolving spiking neural networks for robot control," *Procedia Computer Science*, vol. 6, pp. 329–334, Jan. 2011.
- [28] N. Takase, J. Botzheim, and N. Kubota, "Evolving spiking neural network for robot locomotion generation," in *2015 IEEE Congress on Evolutionary Computation (CEC)*, May 2015, pp. 558–565, iSSN: 1941-0026.
- [29] G. C. H. E. de Croon, H. W. Ho, C. De Wagter, E. van Kampen, B. Remes, and Q. P. Chu, "Optic-Flow Based Slope Estimation for Autonomous Landing," *International Journal of Micro Air Vehicles*, vol. 5, no. 4, pp. 287–297, Dec. 2013.
- [30] H. W. Ho, G. C. H. E. de Croon, E. van Kampen, Q. P. Chu, and M. Mulder, "Adaptive Gain Control Strategy for Constant Optical Flow Divergence Landing," *IEEE Transactions on Robotics*, vol. 34, no. 2, pp. 508–516, Apr. 2018.
- [31] R. B. Stein, "A Theoretical Analysis of Neuronal Variability," *Biophysical Journal*, vol. 5, no. 2, pp. 173–194, Mar. 1965.
- [32] Y.-H. Liu and X.-J. Wang, "Spike-Frequency Adaptation of a Generalized Leaky Integrate-and-Fire Model Neuron," *Journal of Computational Neuroscience*, vol. 10, no. 1, pp. 25–45, Jan. 2001.
- [33] X. Yao, "Evolving artificial neural networks," *Proceedings of the IEEE*, vol. 87, no. 9, pp. 1423–1447, Sep. 1999.
- [34] K. Deb, A. Pratap, S. Agarwal, and T. Meyarivan, "A fast and elitist multiobjective genetic algorithm: NSGA-II," *IEEE Transactions on Evolutionary Computation*, vol. 6, no. 2, pp. 182–197, Apr. 2002.
- [35] H. W. Ho and G. C. H. E. de Croon, "Characterization of Flow Field Divergence for MAVs Vertical Control Landing," in *AIAA Guidance, Navigation, and Control Conference*. San Diego, California, USA: American Institute of Aeronautics and Astronautics, Jan. 2016.
- [36] F.-A. Fortin, F.-M. D. Rainville, M.-A. Gardner, M. Parizeau, and C. Gagn, "DEAP: Evolutionary Algorithms Made Easy," *Journal of Machine Learning Research*, vol. 13, no. Jul, pp. 2171–2175, 2012.
- [37] B. J. Pijnacker Hordijk, K. Y. W. Scheper, and G. C. H. E. de Croon, "Vertical landing for micro air vehicles using event-based optical flow," *Journal of Field Robotics*, vol. 35, no. 1, pp. 69–90, 2018.
- [38] E. Rosten and T. Drummond, "Machine Learning for High-Speed Corner Detection," in *Computer Vision ECCV 2006*, ser. Lecture Notes in Computer Science, A. Leonardis, H. Bischof, and A. Pinz, Eds. Springer Berlin Heidelberg, 2006, pp. 430–443.
- [39] J.-Y. Bouguet, "Pyramidal Implementation of the Affine Lucas Kanade Feature Tracker," 2000.
- [40] K. Y. W. Scheper and G. C. H. E. de Croon, "Abstraction, Sensory-Motor Coordination, and the Reality Gap in Evolutionary Robotics," *Artificial Life*, vol. 23, no. 2, pp. 124–141, May 2017.
- [41] A. Gidon, T. A. Zolnik, P. Fidzinski, F. Bolduan, A. Papoutsis, P. Poirazi, M. Holtkamp, I. Vida, and M. E. Larkum, "Dendritic action potentials and computation in human layer 2/3 cortical neurons," *Science*, vol. 367, no. 6473, pp. 83–87, Jan. 2020.
- [42] F. Paredes-Valls, K. Y. W. Scheper, and G. C. H. E. de Croon, "Unsupervised Learning of a Hierarchical Spiking Neural Network for Optical Flow Estimation: From Events to Global Motion Perception," *IEEE Transactions on Pattern Analysis and Machine Intelligence*, 2019.